Ceramics

A$_2$Zr$_2$O$_7$ (A = Nd, Sm, Gd, Yb) zirconate ceramics with pyrochlore-type structure for high-temperature negative temperature coefficient thermistor

Yige Wang[1], Bo Gao[2,*] , Qian Wang[2], Xiaohui Li[2], Zhi Su[1,*], and Aimin Chang[2,*]

[1] *School of Inorganic Chemistry, Xinjiang Normal University, Ürümqi, People's Republic of China*
[2] *Key Laboratory of Functional Materials and Devices for Special Environments of CAS, Xinjiang Key Laboratory of Electronic Information Materials and Devices, Xinjiang Technical Institute of Physics and Chemistry of CAS, Ürümqi, People's Republic of China*

ABSTRACT

The aim of this paper is to present a novel negative temperature coefficient (NTC) thermistor based on A$_2$Zr$_2$O$_7$ (A = Nd, Sm, Gd, Yb) zirconate ceramics with pyrochlore-type structure for high-temperature application. The zirconate ceramics were synthesized via a solid-state reaction method where rare-earth oxides and ZrO$_2$ were used as starting materials. The physical structures were characterized by X-ray diffraction, scanning electron microscopy, and Raman spectroscopy. It was confirmed that Nd$_2$Zr$_2$O$_7$ and Sm$_2$Zr$_2$O$_7$ are pyrochlore phases, while Yb$_2$Zr$_2$O$_7$ and Gd$_2$Zr$_2$O$_7$ are defect fluorite phases. The electrical property investigated by using resistance–temperature measurements demonstrated that the prepared A$_2$Zr$_2$O$_7$ zirconate ceramics exhibit a typical characteristic of NTC over a wide temperature range between 673 and 1273 K. Particularly, A$_2$Zr$_2$O$_7$, in addition to having high activation energy to ensure better sensitivity, can still maintain higher resistivity under high-temperature environments. Furthermore, the resistivity of A$_2$Zr$_2$O$_7$ is almost independent of the change in oxygen partial pressure. These properties are superior to the classical spinel-type or perovskite-type NTC thermistor, providing valuable information to explore new NTC thermistor for high-temperature applications.

Introduction

With vigorous developments in automotive electronics, military, and aerospace industries, negative temperature coefficient (NTC) thermistors have attracted great attention due to the growing demand for sensing, monitoring, and controlling systems that have high precision and can withstand harsh environments. NTC thermistors, as one of thermally sensitive resistors, exhibit a monotonic decrease in electrical resistance as the temperature increases. It is

Springer

known that NTC ceramic materials are based on solid solution of transition metal oxides, namely Mn, Co, Ni, Fe, Cu, and Zn [1]. However, these materials cannot be used for temperatures over 300°C because of their instability and changing electrical properties at high temperatures. Therefore, the investigation of new high-temperature NTC thermistor materials is imperative.

On the other hand, developing such kinds of materials is not easy. The critical challenge is that they must have high chemical and thermal stability. Also, they have to withstand harsh environments of high pressure and severe oxidation/corrosion, which could be caused by the high temperature. To date, several materials with different structures, such as perovskite [2], spinel [3, 4], pyrochlore [5, 6], polymer-derived [7], and scheelite [8, 9] ceramics, have been investigated for high-temperature NTC thermistor applications. Despite the progress, most reported materials have a maximum upper temperature limit of only 800 °C (supplementary information found in Table S1). A novel hybrid system, hybridizing a less resistive phase with a high resistive phase [10], conferring good NTC performance, is worth mentioning. This system has been used in designing high-temperature thermistor materials recently, whose operating temperature ranges from room temperature to 800°C or even 1000°C. However, due to the poor aging performance of these systems [11–13], especially resistance changes are only a few ohms or tens of ohms when it operates near the ceiling temperature, which restricts their applications. Thus, the investigation of thermistor materials that can be applied in temperatures exceeding 800°C is still urgent.

In the recent decades, pyrochlore compounds with the general formula $A_2B_2O_7$, where A is a trivalent rare-earth element and B is a tetravalent transition metal element, have attracted great attentions [14–17]. These compounds have structures that have high chemical and thermal stability, which can accommodate a wide variety of chemical substitutions and structural defects and provide numerous properties, such as superconductivity [14] and semiconductivity [15]. Thus, they have been considered as candidates for catalysts [16], thermal barrier coatings [17], and solid electrolytes in high-temperature fuel cells [18]. When these compounds are used in the aforementioned applications, it is worth noting that rare-earth-based zirconates with pyrochlore-type structure still maintain stable physical, chemical, thermal properties under harsh environments, including high temperature, high pressure, and severe oxidation/corrosion. Moreover, their electrical properties depend on the composition and the degree of disorder on the cation sites [18] and can be continuously modulated by substitution or doping. These properties make them one of the promising hosts for high-temperature thermistor [5, 6, 19]. However, to the best of our knowledge, there has been no adequate research on the use of rare-earth zirconates with pyrochlore-type structure for NTC thermistors. Therefore, in this paper, we introduce a novel NTC material based on $A_2Zr_2O_7$ (A = Nd, Sm, Gd, Yb) zirconate ceramics with pyrochlore-type structure. Since $A_2Zr_2O_7$ (A = Nd, Sm, Gd, Yb) zirconate ceramics exhibit a wide temperature range between 673 and 1273 K, they are potential candidates for NTC thermistor materials for high-temperature application.

Experimental

$A_2Zr_2O_7$ (A = Sm, Yb, Nd, Gd) ceramics were synthesized via solid-state reaction method. The starting materials were ZrO_2 (purity ≥ 99.9%; Aladdin, Shanghai, China), Sm_2O_3 (purity ≥ 99.9%; Aladdin, Shanghai, China), Yb_2O_3 (purity ≥ 99.9%; Aladdin, Shanghai, China), Nd_2O_3 (purity ≥ 99.9%; Aladdin, Shanghai, China), and Gd_2O_3 (purity ≥ 99.9%; Aladdin, Shanghai, China). The constituent chemicals taken in stoichiometric ratios were ball-milled for 8 h with ethanol as the mixing aid. After being dried at 423 K for 6 h, the mixed powders were uniaxially compacted into disks of 8.5 mm in diameter and 1.5 mm in thickness at 20 MPa and then cold isostatically pressed at 300 MPa for 3 min to form pellets. Finally, the pressureless sintering of as-prepared pellets was performed in a furnace at 1923 K for 10 h in air.

The Archimedes principle was used to measure the densities of the specimens, utilizing deionized water as an immersion medium. The theoretical density of the solid solution was calculated using molecular weight in a unit cell and lattice parameters obtained from the X-ray diffraction (XRD) results. XRD (Bruker D2 PHASER diffractometer, Blue Scientific, UK) using Cu Kα radiation was employed to identify the crystalline phase of the

ceramics. For the Rietveld refinement of the XRD data, analyses were performed in a range of 2θ from 10° to 100° with a step size of 0.01°, and the General Structure Analysis System software was used. The surface morphology of the as-sintered ceramic pellets was observed using a scanning electron microscope (SEM; FEI Quanta 200 SEM, ThermoFisher Scientific, MA, USA). The pellets were first rinsed in an ultrasonic bath of ethanol for 30 min and then were coated with a thin gold film on their surface by vacuum deposition. The Raman spectra were recorded with a micro-Raman spectrometer (NRS1000, Japan Spectroscopic Company, Tokyo, Japan) using an Ar^+ laser (20 mW, 532 nm) as the excitation source in the backscattering configuration. For the characterization of electrical properties, sintered pellets were first rinsed in an ultrasonic bath of ethanol for 15 min, then painted with a conducting platinum paste on both sides, and baked as electrode at 1173 K. Resistance was measured from 673 to 1273 K in the air by using a digital multimeter (Keithley 2000). The resistance was also measured in N_2–O_2 gas mixture with oxygen partial pressures of 10^{-2} and 10^{-3} atm. The measurement was performed in a closed tube furnace, and the oxygen partial pressure was measured and controlled with an yttria-stabilized zirconia oxygen sensor close to the specimens. Aging test was conducted by keeping the pellets in an oven at 1073 K in the air for 300 h. The relative resistance drift of aging pellets was defined by the relationship $\Delta R/R_0 = (R - R_0)/R_0$, where R_0 and R are the resistance at 1073 K before and after aging, respectively.

Results and discussion

Typical surface micrographs of $A_2Zr_2O_7$ (A = Nd, Sm, Gd, Yb) ceramics sintered at 1923 K are displayed in Fig. 1. The surface morphologies of all samples were similar, the microstructures are dense, the grain boundaries are clear, no other phases are formed, and the average grain size is about 5 μm. Relative densities of the $A_2Zr_2O_7$ (A = Nd, Sm, Gd, Yb) ceramics are 97.7%, 96.1%, 96.4%, and 94.9%, respectively.

Figure 2 shows the XRD patterns of $A_2Zr_2O_7$ (A = Nd, Sm, Gd, Yb) ceramics. The XRD pattern of the zirconia is also shown for comparison. The disappearance of the diffraction peak of zirconia

(baddeleyite-type monoclinic zirconium oxide, JCPDS card no. 37-1484) obviously proves that it has been combined with the rare-earth oxide at the sintering temperature. The major diffraction peaks around 2θ = 29°, 34°, 48°, and 57°, for $Nd_2Zr_2O_7$, $Sm_2Zr_2O_7$, $Gd_2Zr_2O_7$, and $Yb_2Zr_2O_7$ ceramics, agree with the literature [5, 6, 19], indicating that the as-prepared zirconate ceramics are identified as single phase. On the other hand, the position of the diffraction peak gradually shifts toward the high-angle region. This is attributed to the shrinkage of the lattice volume, which is caused by the decrease in the radius of A^{3+} cations of $A_2Zr_2O_7$ (A = Nd, Sm, Gd, Yb) ceramics. Furthermore, the XRD patterns for the four ceramics reveal a difference in the presence of typical superlattice peaks at 2θ values of about 14° (111), 28° (311), 37° (331), 45° (511), and 51° (531) [20]. The appearance of superlattice peaks is the characteristic of the pyrochlore phase distinguished from the defect fluorite phase, which is attributed to the ordered arrangement of A^{3+}/Zr^{4+} cations. According to the research by Mandal et al. [21, 22], the structural order degree of these solid solutions is closely related to the ionic radius ratio of $r(A^{3+})/r(Zr^{4+})$. The rare-earth zirconates exhibit a defect fluorite-type structure for $r(A^{3+})/r(Zr^{4+}) < 1.46$ and a pyrochlore-type structure for $r(A^{3+})/r(Zr^{4+}) \geq 1.46$. In $A_2Zr_2O_7$ ceramics, the ionic radius is 0.72 Å for Zr^{4+} in the sixfold coordination. Also the ionic radius is 1.109 Å for Nd^{3+}, 1.079 Å for Sm^{3+}, 1.053 Å for Gd^{3+}, and 0.985 Å for Yb^{3+} in the eightfold coordination [23], in which the value of $r(A^{3+})/r(Zr^{4+})$ corresponds to 1.54, 1.49, 1.46, and 1.36, respectively. Based on the value of $r(A^{3+})/r(Zr^{4+})$ and the presence of superlattice peaks, $Nd_2Zr_2O_7$ and $Sm_2Zr_2O_7$ should be identified in the pyrochlore structure and $Yb_2Zr_2O_7$ should be identified in the defect fluorite structure. Although $r(A^{3+})/r(Zr^{4+})$ of 1.46 indicated that it would incline to form a pyrochlore structure, $Gd_2Zr_2O_7$ exhibits the defect fluorite structure as the sintered temperature is higher than the order/disorder transition temperature (1803 K) [24]. These properties can be further proved from the Rietveld refinement results. Figure 3 shows the Rietveld refinement of the XRD patterns of $A_2Zr_2O_7$ (A = Nd, Sm, Gd, Yb) ceramics after sintering at 1923 K. Profile R factors (Rp, Rwp) and all the extracted parameters from the refinement analysis are summarized in Table 1. The fitting provides good agreement between the experimental and calculated data based

Figure 1 SEM images of $A_2Zr_2O_7$ (A = Nd, Sm, Gd, Yb) samples sintered at 1923 K: **a** $Nd_2Zr_2O_7$, **b** $Sm_2Zr_2O_7$, **c** $Gd_2Zr_2O_7$, and **d** $Yb_2Zr_2O_7$.
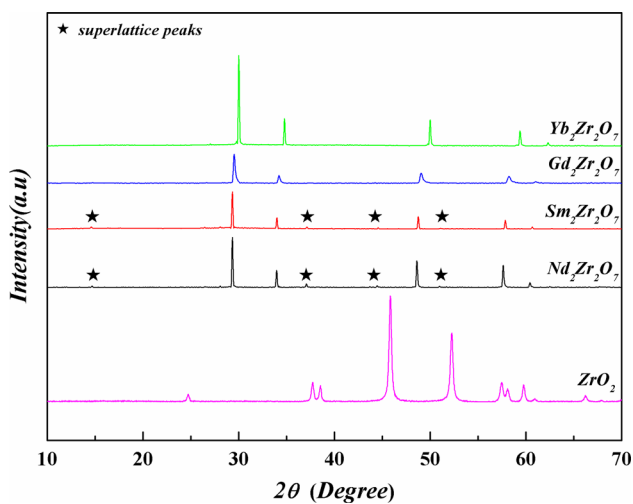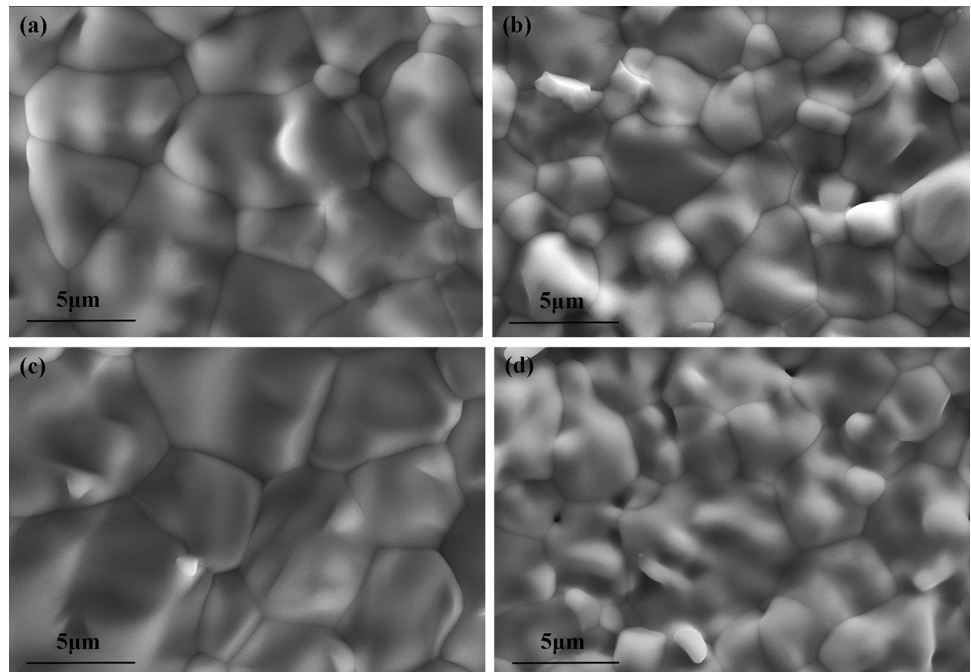

Figure 2 XRD patterns of $A_2Zr_2O_7$ (A = Nd, Sm, Gd, Yb) ceramics and zirconia.

on relatively lower R_p and R_{wp} (< 10%) values, which further confirmed the single-phase pyrochlore structure of $Nd_2Zr_2O_7$ and $Sm_2Zr_2O_7$ and the single-phase defect fluorite structure of $Yb_2Zr_2O_7$ and $Gd_2Zr_2O_7$.

Raman spectroscopy is commonly used because it is more sensitive to the vibration of oxygen ions. Figures 4 and 5 display the Raman spectra of sintered $A_2Zr_2O_7$ (A = Nd, Sm, Gd, Yb) ceramics and their deconvolution results. According to the group theory, pyrochlore $A_2Zr_2O_7$, belonging to the space group $Fd3m$ with Z = 8, has six Raman active modes,

which can be represented as $\Gamma = A_{1g} + E_g + 4F_{2g}$ [25]. As shown in Figs. 4 and 5, for pyrochlore phase, the E_g mode presented at 305 cm^{-1}, F_{2g} mode presented at 405 cm^{-1}, and A_{1g} mode presented at 520 cm^{-1} correspond to the O–A–O bending vibration, Zr–O stretching vibration, and A–O stretching vibration, respectively. It is clear that $Nd_2Zr_2O_7$ can be classified into the pyrochlore structure based on the presence of characteristic Raman active modes. Subsequently, the E_g Raman active mode at 305 cm^{-1} of the other samples becomes broad and weak. This broadening could not be attributed to the smaller particle size because the samples were synthesized via high-temperature sintering route. Furthermore, the XRD patterns are reasonably sharp and the observation from SEM indicates the size of the particles is in the micro-regime. Ordered compounds, like pyrochlore, also have disorder due to the presence of vacancy and defects, which disrupts the translational symmetry in the lattice and, consequently, relaxes the $k \approx 0$ selection rule. Hence, phonons from all parts of the Brillouin zone start contributing to the optical spectra, thereby giving rise to broadened, continuously spread, and weak-intensity bands [26]. In Figs. 4 and 5, a comparison of the Raman spectra indicates that the spectrum of $Sm_2Zr_2O_7$ is similar to that of $Nd_2Zr_2O_7$ with even broader and weaker modes, which indicates a tendency toward disordering of the pyrochlore
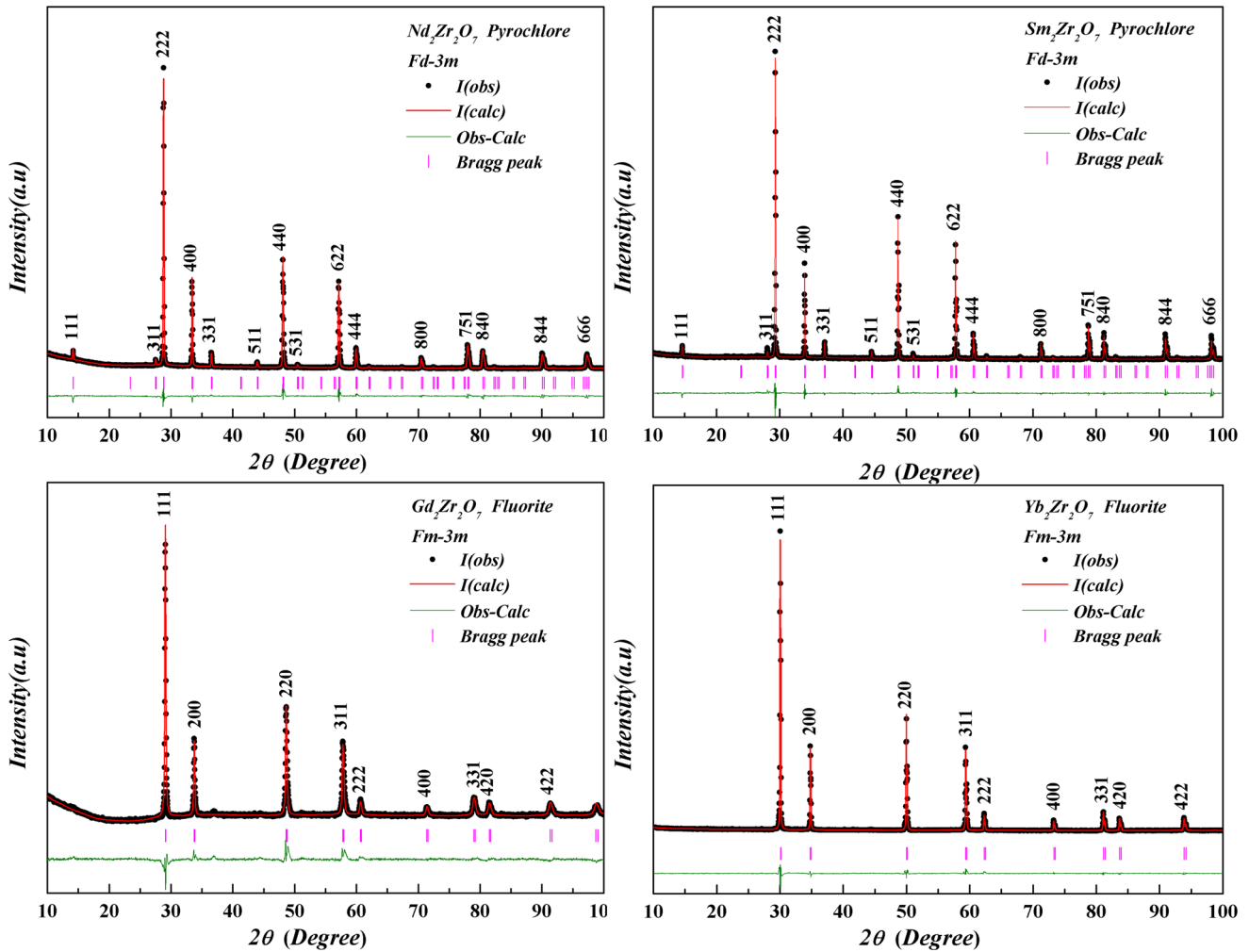
Figure 3 The Rietveld refinement results for the XRD patterns of $A_2Zr_2O_7$ (A = Nd, Sm, Gd, Yb) ceramics after sintering at 1923 K.

structure, giving rise to the defect fluorite structure. However, the spectrum of $Sm_2Zr_2O_7$ still has a characteristic shape, which makes it possible to attribute the anion sublattice to the pyrochlore-type structure, since the cation sublattice becomes disordered earlier than the anion sublattice during the crystallization [27]. In other words, the lattice of $Sm_2Zr_2O_7$ ceramics is supposed to be short-range disordered and long-range ordered [26, 27]. After that, as the radius of cation decreases, the spectra of $Gd_2Zr_2O_7$ and $Yb_2Zr_2O_7$ broaden, and the peak intensity becomes sharply weak, which is accompanied by lattice volume shrinkage (see Table 1). This indicates that there is a tendency to form a disordered pyrochlore-type anion sublattice, which means an ordered/disordered structural transformation happens. Accordingly, the defect fluorite structure of

$Yb_2Zr_2O_7$ and $Gd_2Zr_2O_7$ can be confirmed, which is in accordance with the XRD analysis.

Figure 6 shows the natural logarithm of the resistivity (ρ) as a function of the reciprocal temperature (1000/T). For all curves, the resistivity decreases exponentially as the temperature increases, indicating a typical NTC characteristic. This can be attributed to the characteristic that the dominant ion diffusion in zirconate is a thermal activation process [28]. It is, therefore, reasonable to believe that the oxygen vacancy-hopping diffusion will be improved at elevated temperature, resulting in the reduction of resistivity, thereby giving the NTC effect. Furthermore, it is evident that a linear relationship between these two parameters exists over the range of 673 K–1273 K, which conforms to the classical Arrhenius relationship: $\rho = \rho_o \exp(-E_a/kT)$ [28]. ρ_o is the resistivity of the material at infinite temperature, T is the

Table 1 Summary of the results obtained from the Rietveld refinement of the XRD patterns for $A_2Zr_2O_7$ (A = Nd, Sm, Gd, Yb) ceramics

Sample	$a = b = c$ (Å), $\alpha = \beta = \gamma = 90°$									R_p	R_{wp}
	Space group	Atom	Atom positions			Wyck.	s.o.f	Lattice parameter (Å)	Lattice volume (Å³)		
			x	y	z						
$Nd_2Zr_2O_7$	Fd-3m (227)	Nd1	0.5	0.5	0.5	16d	1	10.64327	1205.661	5.10	4.37
		Zr2	0	0	0	16c	1				
		O3	0.33506	0.125	0.125	48f	1				
		O4	0.375	0.375	0.375	8b	1				
$Sm_2Zr_2O_7$	Fd-3m (227)	Sm1	0.5	0.5	0.5	16d	1	10.59987	1190.972	4.14	2.84
		Zr2	0	0	0	16c	1				
		O3	0.33174	0.125	0.125	48f	1				
		O4	0.375	0.375	0.375	8b	1				
$Gd_2Zr_2O_7$	Fm-3m (225)	Gd1	0	0	0	4a	0.5	5.26243	145.733	4.15	2.67
		Zr1	0	0	0	4a	0.5				
		O1	0.25	0.25	0.25	8c	0.875				
$Yb_2Zr_2O_7$	Fm-3m (225)	Yb1	0	0	0	4a	0.5	5.17131	138.294	5.58	3.83
		Zr2	0	0	0	4a	0.5				
		O3	0.25	0.25	0.25	8c	0.875				

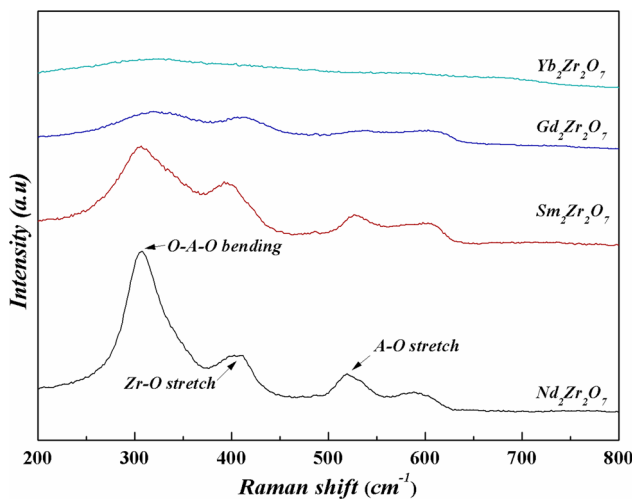*Wyck.* Wyckoff positions, *s.o.f* site occupancy factor

Figure 4 Raman spectra of sintered $A_2Zr_2O_7$ (A = Nd, Sm, Gd, Yb) ceramics.

absolute temperature, k is the Boltzmann constant and E_a is the activation energy for electrical conduction that can be calculated from the slopes of the $\ln\rho$ versus $1/T$ plots. In addition, the thermistor constant B and temperature coefficient of resistance α, which indicates sensitivity to temperature excursions, are given in the following equations:

$$B = [(T_1 \times T_2)/(T_2 - T_1)]/\text{Ln}(R_1/R_2) \quad (1)$$

$$\alpha_T = (1/\rho)(\partial_\rho/\partial_T) = -B/T^2 \quad (2)$$

where R_1 and R_2 are the resistance of the thermistor at temperatures T_1 and T_2, respectively. The values of ρ_{1273K}, B constant, α_T, and E_a, as well as the relative resistance drift after aging at 1073 K in air for 300 h are listed in Table 2. It can be seen from Fig. 6 and Table 2 that all electrical parameters increase as $r(A^{3+})/r(Zr^{4+})$ decreases. Particularly, the ρ_{1273K} of $Nd_2Zr_2O_7$ and $Sm_2Zr_2O_7$ with pyrochlore phase is significantly lower than that of $Gd_2Zr_2O_7$ and $Yb_2Zr_2O_7$ with the defect fluorite phase. This means the size of the ionic radius of A^{3+} has a decisive influence on the conductivity of $A_2Zr_2O_7$ (A = Nd, Sm, Gd, Yb) ceramics. Wilde and Catlow [29] reported that in the pyrochlore, the diffusion mechanism underlying the conductivity is dominated by oxygen ion vacancy hopping along the 48f sites. This because only the 48f sites always have 8b, 8a and 48f sites as second nearest neighbours in detailed structure of $A_2Zr_2O_7$, and these adjacent 48f sites can finally form a continuous chain along which oxygen vacancy-hopping diffusion could take place. As indicated by the XRD and Raman analyses, $A_2Zr_2O_7$ (A = Nd, Sm, Gd, Yb) ceramics have a tendency to form the disordered structure as the radius of A^{3+} cations decreases, which means the number of 48f oxygen vacancy decreases. The reduction in oxygen vacancies will undoubtedly increase the energy barrier for oxygen
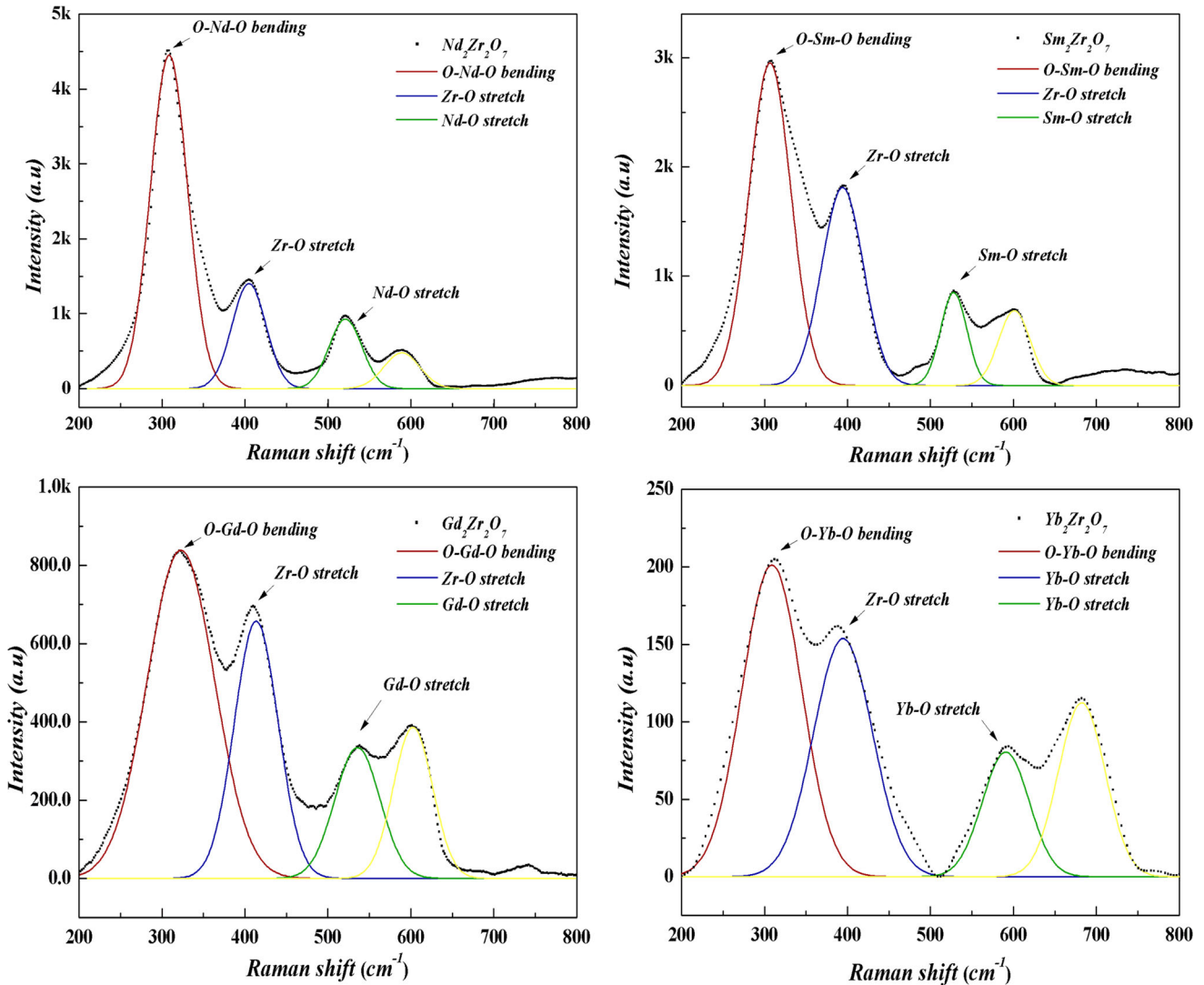
Figure 5 Deconvolution results of Raman spectra for $A_2Zr_2O_7$ (A = Nd, Sm, Gd, Yb) ceramics.

ion 48f vacancy hopping, thereby resulting in the increase of electrical resistivity and activation energy in the sequence of $Nd_2Zr_2O_7$, $Sm_2Zr_2O_7$, $Gd_2Zr_2O_7$, and $Yb_2Zr_2O_7$.

In addition, the sensitivity of NTC thermistors can be defined in the following equation because of $B = E_a/k$: $\quad \alpha_T = (1/\rho)(\partial_\rho/\partial_T) = - B/T^2 = - E_a/(kT^2)$. This equation indicates that the larger the E_a and constant B, the higher is the α_T of a thermistor. Since α_T exponentially decreases with the temperature factor of T^{-2}, there is a gradual decrease in sensitivity as temperature arises. Therefore, it is required that thermistors should have high E_a and constant B to maintain high sensitivity at high temperatures. As shown in Table 2, although the calculated E_a and constant B of zirconate ceramics decrease as $r(A^{3+})/$

$r(Zr^{4+})$ increases, the values obtained are much higher compared to high-temperature NTC materials reported in the literature [2, 30–34], almost more than twice as high. As a consequence, $Yb_2Zr_2O_7$ has α_T values as high as − 2.353%/K at 773 K and − 1.022%/K at 1173 K, indicating better precision in high-temperature measurements. Even $Nd_2Zr_2O_7$ with the lowest value of E_a and constant B has α_T values of − 1.642%/K at 773 K and − 0.713%/K at 1173 K, nearly twice than that of the perovskite-based NTC materials [1, 2, 10, 30–34]. Therefore, this nature evidently makes $A_2Zr_2O_7$ (A = Nd, Sm, Gd, Yb) ceramics retain a sufficient sensitivity, allowing extended application at high temperatures. Moreover, as listed in Table 2, the relative resistance drift of $A_2Zr_2O_7$ (A = Nd, Sm, Gd, Yb) ceramics was in the

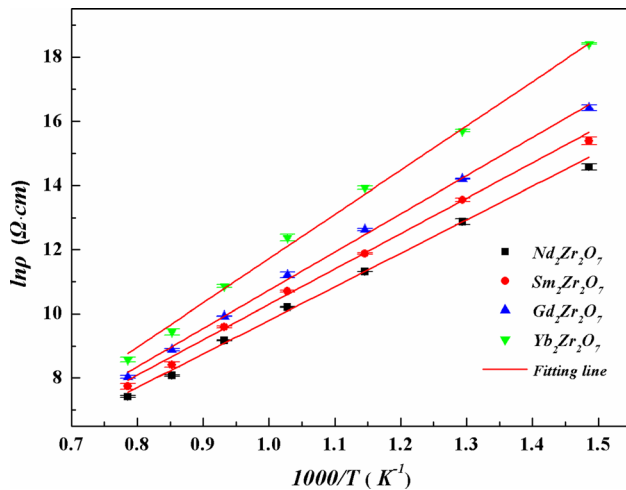**Figure 6** The resistivity of $A_2Zr_2O_7$ (A = Nd, Sm, Gd, Yb) ceramics as a function of temperature.

Figure 7 Experimental data ($Ln\rho$) from earlier studies [2, 10, 30–34] at the upper temperature limit compared with $A_2Zr_2O_7$ (A = Nd, Sm, Gd, Yb) ceramics.

range of 0.34–4.23% after aging at 1073 K in the air for 300 h, possessing better aging stability compared with the perovskite-type structural high-temperature NTC ceramics materials [11–13]. Therefore, both sufficient sensitivity and good aging stability make $A_2Zr_2O_7$ (A = Nd, Sm, Gd, Yb) ceramics candidates for high-temperature NTC materials.

Figure 7 shows the resistivity at the upper temperature limit obtained from recent progress in high-temperature NTC materials, including $YCr_{0.8}Mn_{0.2}O_3$ [2], Y_2O_3–$YCr_{0.5}Mn_{0.5}O_3$ [10], $Bi_3Zn_2Sb_2O_{14}$ [30], $0.6MgAl_2O_4$–$0.4LaCr_{0.5}Mn_{0.5}O_3$ [31], $Sr_7Mn_4O_{15}$ [32], Bi_2O_3–WO_3–Ta_2O_5–TiO_2 [33], and $BaTiO_3$ + $BaBiO_3$ [34]. For the sake of comparison, the experimental data of our work are also provided. As indicated previously, most materials reported a maximum upper-temperature limit of only 800°C. Although the novel hybrid systems, such as $0.6MgAl_2O_4$–$0.4LaCr_{0.5}Mn_{0.5}O_3$ [31] and Y_2O_3–$YCr_{0.5}Mn_{0.5}O_3$ [10], claimed an upper temperature limit as high as 1000°C, both resistance values and its changes are only several or tens of ohms, which still restricted their practical application. As we have known, for practical applications, the circuit design of the NTC thermistor usually requires a resistance value change
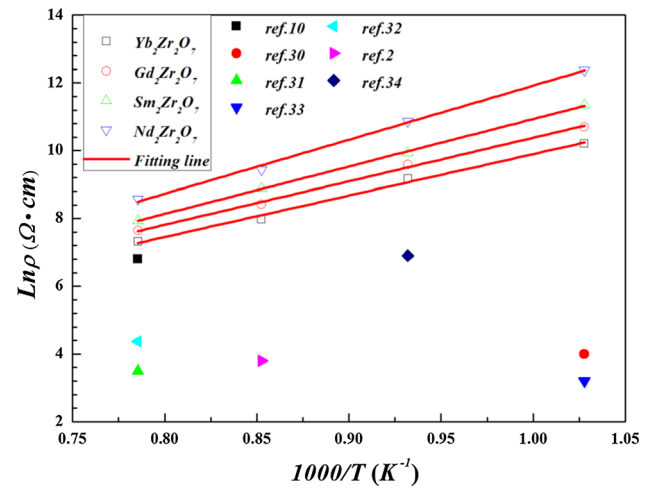
within a certain range (commonly from 100 Ω to 100 kΩ) in order to select a suitable operating temperature range. Therefore, the NTC material has the ability to maintain high resistivity at high temperature, which is a key factor. From Fig. 6 and Table 2, it is noteworthy that the value of resistivity for each zirconate is much larger than that reported in the literature, and it is often several times or even an order of magnitude higher at the same temperature [2, 10, 30–34]. This, coupled with the high E_a, helps designing the NTC thermistor that can really achieve a temperature up to 800°C or even 1000°C. Furthermore, as shown in Fig. 8, by comparing the resistivity of $A_2Zr_2O_7$ (A = Nd, Sm, Gd, Yb) ceramics in air and an atmosphere with different oxygen partial pressures at 1073 K, we find that their resistivities are almost independent of change in the oxygen partial pressure. This may be due to the oxide-ion conduction characteristics of zirconate, where ionic diffusion in this series is dominant and only thermally activated, while electronic conduction is negligible [28]. We will further carry out this works concentrating on why the zirconate ceramics retain a stable electrical characteristic under different oxygen partial pressures. But even so, this oxygen-insensitive characteristic is

Table 2 Electrical parameters of $A_2Zr_2O_7$ (A = Nd, Sm, Gd, Yb) ceramics

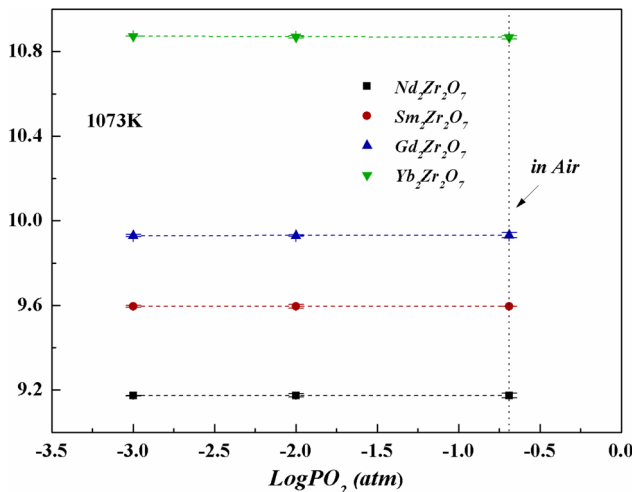| Sample	ρ_{1273K} (Ω cm)	$B_{673/1273}$ (K)	E_a (eV)	α_{773K} (%/K)	α_{1173K} (%/K)	$\Delta R/R$ (%)	$r(A^{3+})/r(Zr^{4+})$
$Nd_2Zr_2O_7$	1512.52	9812	0.8456	− 1.642	− 0.713	0.34	1.54
$Sm_2Zr_2O_7$	2094.92	10781	0.9290	− 1.804	− 0.784	4.23	1.49
$Gd_2Zr_2O_7$	2809.85	12117	1.0441	− 2.028	− 0.881	2.48	1.46
$Yb_2Zr_2O_7$	5289.09	14060	1.2116	− 2.353	− 1.022	3.23	1.36

Figure 8 Oxygen partial pressure dependence of electrical resistivity for $A_2Zr_2O_7$ (A = Nd, Sm, Gd, Yb) ceramics.

superior to the classical spinel-type or perovskite-type NTC thermistor because the resistivity of such oxides has a close relationship with oxygen partial pressure [10, 35]. These results mean that, in addition to being applicable to air, zirconate ceramics may also have a potential application in high-temperature environments with oxidation/reduction, providing valuable information to explore new high-temperature NTC thermistor.

Conclusions

Novel high-temperature NTC thermistor materials based on $A_2Zr_2O_7$ (A = Nd, Sm, Gd, Yb) zirconate ceramics with pyrochlore-type structure are synthesized via solid-state reaction method. Electrical measurements confirm that the prepared ceramics exhibit a typical NTC characteristic over a wide temperature range between 673 and 1273 K. It is also found that, in addition to high E_a, $A_2Zr_2O_7$ can maintain high resistivity under high-temperature environment, and the resistivity is almost independent of the change in oxygen partial pressure. These properties are superior to the classical spinel-type or perovskite-type NTC thermistor, providing valuable information to further explore new high-temperature NTC thermistor.

Acknowledgements

Compliance with ethical standards

Conflict of interest The authors declare that they have no conflict of interest.

Electronic supplementary material: The online version of this article (https://doi.org/10.1007/s108 53-020-05104-5) contains supplementary material, which is available to authorized users.

References

[1] Feteira A (2009) Negative temperature coefficient resistance (NTCR) ceramic thermistors: an industrial perspective. J Am Ceram Soc 92:967–983

[2] Kamlo AN, Bernard J, Lelievre C, Houivet D (2011) Synthesis and NTC properties of $YCr_{1-x}Mn_xO_3$ ceramics sintered under nitrogen atmosphere. J Eur Ceram Soc 31:1457–1463

[3] Metz R (2000) Electrical properties of N.T.C. thermistors made of manganite ceramics of general spinel structure: $Mn_{3-x-x'}M_xN_{x'}O_4$ ($0 \leq x+x' \leq 1$; M and N being Ni, Co or Cu). Aging phenomenon study. J Mater Sci 35:4705–4711. https://doi.org/10.1023/A:1004851022668

[4] De Vidales JLM, Garcia-Chain P, Rojas RM, Vila E, Garcia-Martinez O (1998) Preparation and characterization of spinel-type Mn-Ni-Co-O negative temperature coefficient ceramic thermistors. J Mater Sci 33:1491–1496. https://doi.org/10.1023/A:1004351809932

[5] Sumi S, Rao PP, Koshy P (2014) Manganese double substituted pyrochlore type semiconducting oxides for high temperature NTC thermistor applications. J Mater Sci Mater Electron 25:2985–2991

[6] Nobre MAL, Lanfredi S (2003) Negative temperature coefficient thermistor based on $Bi_3Zn_2Sb_3O_{14}$ ceramic: an oxide semiconductor at high temperature. Appl Phys Lett 82:2284–2286

[7] Yu YX, Huang QF, Rhodes S, Fang JN, An LN (2017) SiCNO-GO composites with the negative temperature coefficient of resistance for high-temperature sensor applications. J Am Ceram Soc 100:592–601

[8] Deepa M, Rao PP, Sumi S, Radhakrishnan ANP, Koshy P (2010) New negative temperature coefficient ceramics in Ca-Ce-Nb-M-O (M = Mo or W) system. J Am Ceram Soc 93:1576–1579

[9] Zhang B, Zhao Q, Zhao CJ, Chang AM (2017) Comparison of structure and electrical properties of vacuum-sintered and conventional-sintered $Ca_{1-x}Y_xCeNbWO_8$ NTC ceramics. J Alloy Compd 698:1–6

[10] Houivet D, Bernard J, Haussonne JM (2004) High temperature NTC ceramic resistors (ambient-1000°C). J Eur Ceram Soc 24:1237–1241

[11] Yokokawa H, Natsuko S, Tatsuya K, Dokiya M (1991) Chemical thermodynamic considerations in sintering of $LaCrO_3$-based perovskites. J Electrochem Soc 138:1018–1027

[12] Peck DH, Miller M, Kobertz D, Nickel H, Hilpert K (1996) Vaporization of $LaCrO_3$: partial and integral thermodynamic properties. J Am Ceram Soc 79:3266–3272

[13] Takeuchi T, Takeda Y, Funahashi R, Aihara T, Tabuchi M, Kageyama H (2000) Rapid preparation of dense $(La_{0.9}Sr_{0.1})CrO_3$ ceramics by spark-plasma sintering. J Electrochem Soc 147:3979–3982

[14] Sakai H, Yoshimura K, Ohno H, Kato H, Kambe S, Walstedt RE, Matsuda TD, Haga Y (2004) Superconductivity in a pyrochlore oxide, $Cd_2Re_2O_7$. J Phys: Condens Matter 16:L9–L12

[15] Deepa M, Rao PP, Sumi S, Radhakrishnan AN, Chandran MR, Koshy P (2011) Structural and electrical properties of nonstoichiometric semiconducting pyrochlores in Ca-Ce-Ti-Nb-O system. Mater Chem Phys 127:162–169

[16] Sohn JM, Kim MR, Woo SI (2003) Characterization of $Ln_2B_2O_7$ (Ln = Sm, Eu, Gd, and Tb; B = Ti or Zr) with pyrochlore structure as novel CH_4 combustion catalyst. Catal Today 83:289–297

[17] Vassen R, Cao XQ, Tietz F, Basu D, Stover D (2000) Zirconates as new materials for thermal barrier coatings. J Am Ceram Soc 83:2023–2028

[18] Xia XL, Liu ZG, Ouyang JH (2011) Order–disorder transformation and enhanced oxide-ionic conductivity of $(Sm_{1-x}Dy_x)_2Zr_2O_7$ ceramics. J Power Sources 196:1840–1846

[19] Nobre MAL, Lanfredi S (2003) Grain boundary electric characterization of $Zn_7Sb_2O_{12}$ semiconducting ceramic: a negative temperature coefficient thermistor. J Appl Phys 93:5576–5582

[20] Mandal BP, Tyagi AK (2007) Preparation and high temperature-XRD studies on a pyrochlore series with the general composition $Gd_{2-x}Nd_xZr_2O_7$. J Alloy Compd 437:260–263

[21] Subramanian MA, Aravamudan G, Rao GVS (1983) Oxide pyrochlores-a review. Prog Solid State Chem 15:55–143

[22] Subramanian MA, Sleight AW (1993) Chapter 107: Rare earth pyrochlores. In: Gschneidner KA Jr, Eyring L (eds) Handbook on the physics and chemistry of rare earths. Elsevier, Amsterdam, pp 225–248

[23] Rohrer GS (2001) Structure and bonding in crystalline materials. Cambridge University Press, Cambridge, pp 521–525

[24] Michel D, Jorba MP, Collongues R (1974) Etude de la transformation ordre-desordre de la structure fluorite a la structure pyrochlore pour des phases $(1-x)ZrO_2-xLn_2O_3$. Mater Res Bull 9:1457–1468

[25] Glerup M, Nielsen OF, Poulsen FW (2001) The Structural Transformation from the Pyrochlore Structure, $A_2B_2O_7$, to the Fluorite Structure, AO_2. Studied by Raman spectroscopy and defect chemistry modeling. J Solid State Chem 160:25–32

[26] Blanchard PER, Clements R, Kennedy BJ, Ling CD, Reynolds E, Avdeev M, Stampfl APJ, Zhang Z, Jang LY (2012) Does local disorder occur in the pyrochlore zirconates? Inorg Chem 51:13237–13244

[27] Popov VV, Menushenkov AP, Ivanov AA, Gaynanov BR, Yastrebtsev AA, d'Acapito F, Puri A, Castro GR, Shchetinin IV, Zheleznyi MV, Zubavichus YV, Ponkratov KV (2019) Comparative analysis of long- and short-range structures features in titanates $Ln_2Ti_2O_7$ and zirconates $Ln_2Zr_2O_7$ (Ln = Gd, Tb, Dy) upon the crystallization process. J Phys Chem Solids 130:144–153

[28] Goodenough JB (2000) Ceramic technology: oxide-ion conductors by design. Nature 404:821–823

[29] Wilde PJ, Catlow CRA (1998) Defects and diffusion in pyrochlore structured oxides. Solid State Ionics 112:173–183

[30] Nobre MAL, Lanfredi S (2002) The effect of temperature on the electric conductivity property of $Bi_3Zn_2Sb_3O_{14}$ pyrochlore type phase. J Mater Sci Mater Electron 13:235–238

[31] Zhang B, Zhao Q, Chang AM, Wu YQ, Li HY (2016) Spark plasma sintering of $MgAl_2O_4$-$LaCr_{0.5}Mn_{0.5}O_3$ composite thermistor ceramics and a comparison investigation with conventional sintering. J Alloy Compd 675:381–386

[32] Feltz A, Kriegel R, Polzl W (1999) $Sr_7Mn_4O_{15}$ ceramics for high temperature NTC thermistors. J Mater Sci Lett 18:1693–1695

[33] Basu A, Brinkman AW, Hashemi T (2001) NTC characteristics of bismuth based ceramic at high temperature. Int J Inorg Mater 3:1219–1221

[34] Luo Y, Liu XY (2005) High temperature NTC $BaTiO_3$-based ceramic resistors. Mater Lett 59:3881–3884

[35] Banerjee A, Akbar SA (2005) A new method for fabrication of stable and reproducible yttria-based thermistors. Sensor Actuator A Phys 87:60–66